High-Resolution Parameter Estimation for Time-Varying Double Directional V2V Channel

Rui Wang, *Student Member, IEEE*, Olivier Renaudin, *Member, IEEE*, C. Umit Bas, *Student Member, IEEE*, Seun Sangodoyin, *Student Member, IEEE*, and Andreas F. Molisch, *Fellow, IEEE*

***Abstract*— This paper describes a high-resolution parameter estimation algorithm applied to the vehicle-to-vehicle (V2V) multi-dimensional channel measurements. The algorithm, which is based on a maximum likelihood estimator, jointly estimates parameters of multipath components, such as time-of-arrival, direction of departure, direction of arrival, and Doppler shift. It serves to provide a comprehensive understanding of the V2V propagation channel. We propose computationally attractive methods to initialize parameters in the global search and evaluate key components in the local optimization. We also apply the algorithm to actual V2V channel measurement data. The results suggest an overall good performance of the estimator, where 80% of the snapshots have a diffuse power ratio less than 20% and the dominant specular paths match well with the environment and dynamics of the measurement.**

***Index Terms*— V2V, time-varying, MIMO channel sounding measurements, high-resolution parameter estimation.**

I. Introduction

MOTIVATED by the benefits of intelligent transport systems (ITSs), research on vehicle-to-vehicle (V2V) communication technology has proliferated in recent years. It is envisioned that all vehicles on the road can gather data about traffic and road conditions, and exchange these data among themselves or with the road infrastructure. Through exchanging the information, the vehicles may improve their braking aid and lane assist systems, which leads a lower accident rate. The vehicles can also keep a shorter distance between each other, which helps reduce the fuel consumption and traffic jams. Reliable and low-latency communications are a vital prerequisite for these applications.

Channel measurement and modeling are prerequisites for designing and improving communication systems [1]. Most of the V2V measurements, e.g. [2]–[6], focus on canonical channel metrics, such as path-loss, signal fading (large or small scale fading), delay spread and Doppler spread, which characterize the channel with some "bulk" features. However the safety applications in V2V communication demand a high level of robustness in the system design, and thus a more accurate model of the propagation channel it operates in. There is a rich literature on V2V channel modeling as well, see the survey papers [7], [8] and references therein. Most of the V2V channel models fall into these three categories, deterministic models, stochastic models, geometric-based stochastic channel models (GSCMs). All these models require the support of measurements to either calibrate or parameterize the model.

A complete and more accurate characterization of the radio channel requires a multiple-input multiple-output (MIMO) channel sounder equipped with antenna arrays at both transmitter (Tx) and receiver (Rx). Some V2V measurements do use a MIMO sounder, but few papers utilize it to extract the directional information about multipath components (MPCs), which could have provided a deeper insight into the interactions of radio waves with the environment. Reference [9] introduces results on V2V measurements conducted in Lund, Sweden. The channel sounder has a 4×4 MIMO array, and measures at 5.2 GHz with a 240 MHz bandwidth. Its path extraction and tracking algorithm focuses on the delay and signal strength of MPCs, however the angular and Doppler parameters of MPCs are not included in the analysis. Reference [10] proposes a V2V channel model based on measurements conducted in Helsinki, Finland. The channel sounder is equipped with a 30×30 MIMO array and measures at 5.3 GHz with a 60 MHz bandwidth. Its main limitation is the low measurement snapshot rate, which leads a maximal resolvable Doppler about 7.15 Hz and prevents the capability to measure a fast time-varying channel. The path extraction method mainly follows a sequential search and subtract procedure, which is similar to the one introduced in [9]. Besides, the analysis does not report the angular or Doppler characteristics of MPCs. Reference [11] reports the analysis on V2V measurements with a high-resolution parameter estimation (HRPE) algorithm, which jointly estimates all parameters of MPCs. It uses the SAGE algorithm [12] to extract parameters of 50 MPCs with a full-polarimetric setup. However the complexity of SAGE forces the author to reduce the bandwidth to 20 MHz from 240 MHz. Meanwhile only a subset of the snapshots are evaluated, which leads to an effective snapshot rate of 2 Hz. This could compromise the possibility of analyzing the dynamic statistics of MPCs in the V2V channel. To the best of our knowledge, there are no efficient HRPE schemes published to jointly estimate the parameters of specular paths

Manuscript received November 12, 2016; revised May 28, 2017; accepted August 8, 2017. Date of publication August 29, 2017; date of current version November 9, 2017. This work was supported in part by CalTrans through the METRANS framework and in part by the National Science Foundation. The work of O. Renaudin was supported by the Belgian Fonds Spécial de la Recherche Scientifique. The associate editor coordinating the review of this paper and approving it for publication was Z. Sun. *(Corresponding author: Rui Wang.)*

R. Wang, C. U. Bas, S. Sangodoyin, and A. F. Molisch are with the Ming Hsieh Department of Electrical Engineering, University of Southern California, Los Angeles, CA 90089 USA (e-mail: wang78@usc.edu; cbas@usc.edu; sangodoy@usc.edu; molisch@usc.edu).

O. Renaudin was with the University of Southern California, Los Angeles, CA 90089 USA. He is now with the Digital Safety and Security Department, Austrian Institute of Technology, A-1220 Vienna, Austria (e-mail: olivier.renaudin@ait.ac.at).

Color versions of one or more of the figures in this paper are available online at http://ieeexplore.ieee.org.

Digital Object Identifier 10.1109/TWC.2017.2744628

(SP)s and diffuse multi-path components (DMC) in the V2V channel, and our work attempts to close the gap.

A full parametrization of the channel model has to rely on channel measurements, whose evaluations in turn require efficient and robust methods for a multi-dimensional parameter estimation. Most of the HRPE algorithms rely on the maximum likelihood estimator (MLE), which greatly enhances the resolution and accuracy by fitting an appropriate data model to the measurement data. Over the past two decades, a variety of HRPEs has been developed for various applications. ESPRIT is a subspace method but it relies on a special antenna array structure and does not apply to a general case. SAGE builds on the Expectation Maximization (EM) algorithm, which tends to show a slow convergence and in its conventional version neglects the contributions from DMC. A highly accurate method is RIMAX [13], which estimates the parameters of both SP and DMC. To improve the convergence rate, RIMAX uses the Levenberg-Marquardt method [14], [15] in the nonlinear optimization stage for all SPs' parameters. Reference [16] introduces a MPC tracker based on the extended Kalman filter (EKF). However the main data model utilized by RIMAX and EKF assumes the channel is completely static within one MIMO snapshot, which does not hold in general for V2V MIMO channel measurements. Besides, both of them have shortcomings in their initialization methods of SPs. The initialization for RIMAX in [13] implements a sequential search in multiple parameter domains to reduce the computational complexity. Its main drawback is the loss of correlation gain, because samples from various data domains are processed independently. This leads to a higher probability of producing "ghost" paths due to imperfect signal cancellation. In contrast reference [16] exploits the full correlation gain by jointly initializing all structural for one SP, but its computational complexity becomes prohibitive when we are facing large multidimensional measurements.

Our work relies on the double-directional channel model [17], and models the channel impulse response as a sum of contributions from plane waves. This underlying signal model provides not only insights into the directional characteristics of the V2V channel, but also a framework that allows a joint estimation of all parameters related to MPCs. Our adopted data model also captures the phase envolution within one MIMO measurement, which is the most suitable for the time-varying V2V channel. We develop an HRPE scheme based on the framework of RIMAX in [13]. Special attention is paid to improve the numerical implementation, such as the initialization of the parameters of SPs, the score function and Fisher Information Matrix (FIM). The efficient initialization method is an extension of our conference paper [18]. To validate our proposed estimation algorithm, we build a dedicated real-time channel sounder suitable for V2V channels, and conduct extensive measurement campaigns. To the best of our knowledge, this is the first published work with optimized implementation that jointly estimates all parameters of MPCs and DMC from V2V channel measurements.

The main contributions of this work are the following:

- we find a suitable signal data model for V2V MIMO channel measurements, which enables evaluations with an HRPE algorithm based on the framework of RIMAX;
- we propose computationally attractive methods to initialize parameters of SPs, and to evaluate the score function and FIM in the nonlinear optimization stage;
- we validate the data model and the HRPE algorithm with a self-built V2V channel sounder and actual V2V measurement data.

The remainder of the paper is organized as follows. Section II introduces the general data model of the estimator. Section III introduces a simplified model catering to our setup for V2V channel measurement and efficient methods for the numerical implementation. In Section IV we present simulation results based on synthetic channel responses and some sample results based on our V2V measurement data. In Section V we draw the conclusions.

The symbol notation used in this paper follows the rules below:

- Bold upper case letters, such as $\mathbf{B}$, denote matrices. $\mathbf{B}()$ represents a matrix valued function.
- Bold lower case letters, such as $\mathbf{b}$, denote column vectors. $\mathbf{b}_j$ is the jth column of the matrix $\mathbf{B}$. $\mathbf{b}()$ stands for a vector valued function.
- Calligraphic upper-case letters denote higher dimensional tensors.
- $[\mathbf{B}]_{ij}$ denotes the element in the ith row and jth column of the matrix $\mathbf{B}$.
- Superscripts *, ^{T} and † denote complex conjugate, matrix transpose and Hermitian transpose.
- The operators $|f(\mathbf{x})|$ and $\|\mathbf{b}\|$ denote the absolute value of a scalar-valued function $f(\mathbf{x})$, and the L2-norm of a vector $\mathbf{b}$.
- The operators $\otimes$, $\odot$ and $\diamond$ denote Kronecker, Schur-Hadamard, and Khatri-Rao products.
- The operator $\oslash$ represents the element-wise division between either two vectors, matrices or tensors, and the operator $\circ$ is the outer product of two vectors.
- The operators $\lfloor\,\rfloor$ and $\lceil\,\rceil$ are the floor and ceiling functions.

II. Signal Data Model

A. Double Directional Channel Model

Reference [17] proposes a channel model that captures the spatial and temporal information of the wireless MIMO channel. The channel response is modeled as a superposition of P plane waves or SPs, whose features are delay τ_p, direction of departure (DoD) $\Omega_{T,p}$, direction of arrival (DoA) $\Omega_{R,p}$, and Doppler shift ν_p. We can divide the DoD into the azimuthal DoD $\varphi_{T,p}$ and elevation DoD $\theta_{T,p}$, and similarly DoA into the azimuth $\varphi_{R,p}$ and elevation $\theta_{R,p}$. The time-varying double directional transfer function is given by

$$\mathbf{H}(f,t) = \sum_{p=1}^{P} \mathbf{b}_R(\Omega_{R,p})^T \mathbf{\Gamma}_p \mathbf{b}_T(\Omega_{T,p}) \cdot e^{-j2\pi(f\tau_p - \nu_p t)}, \quad (1)$$

where $\mathbf{b}_R$ and $\mathbf{b}_T$ are polarimetric antenna array responses for the receiver and the transmitter. $\mathbf{\Gamma}_p$ is the polarimetric path

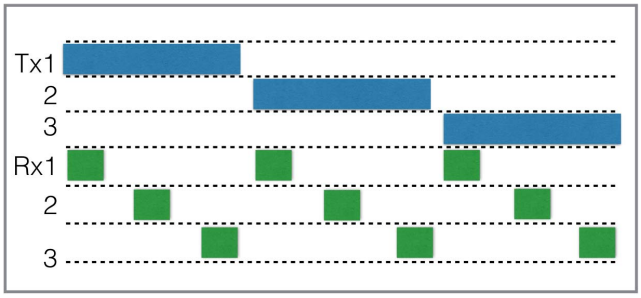

Fig. 1. An example of the sequential switching scheme of a channel sounder equipped with a 3×3 MIMO array.

weight matrix and further defined by

$$\mathbf{\Gamma}_p = \begin{bmatrix} \gamma_{HH,p} & \gamma_{VH,p} \\ \gamma_{HV,p} & \gamma_{VV,p} \end{bmatrix} \tag{2}$$

The subscript of various γ_p denotes the signal polarization, for example HH is horizontal-to-horizontal and VH is vertical-to-horizontal.

B. MIMO Channel Sounding Data Model

Most of the state-of-the-art channel sounders use switched arrays to ensure the highest phase stability during MIMO channel measurements, which is essential for evaluating MIMO measurements with any HRPE algorithm [19]. As a result, this type of channel sounder needs a time division scheduling scheme to collect data between all antenna pairs. Let us consider a series of MIMO snapshots with M_T Tx antennas, M_R Rx antennas, and hence altogether $M_T M_R$ single-input single-output (SISO) channels. If we transmit with a multi-tone sounding signal, one SISO channel consists of M_f frequency points. The dimension of one MIMO snapshot is $M_f \times M_R \times M_T$.

We assume the channel sounder applies a sequential switching scheme illustrated in Fig. 1, and the same sounding sequence of length $\tau_{\max}$ is repeated for each Tx-Rx antenna pair, hence each MIMO snapshot is $T_0 = 2M_R M_T \tau_{\max}$ long. The maximal absolute resolvable Doppler shift without ambiguities is $1/(2T_0)$. However the input to our proposed estimation scheme consists of T MIMO snapshots compared to one MIMO snapshot in [16]. A large value of T increases the observation aperture in the time domain and effectively improves the estimation accuracy of Doppler shifts, which are important in typical V2V channels. Another important assumption of our work is that all structural parameters, including time delay of arrival (TDoA) τ, DoD Ω_T, DoA Ω_R, and Doppler shift ν of SPs, are constant within such T MIMO snapshots. Their timespan is 18.6 ms in our channel sounder setup [20]. Moreover we assume the complex path weights of SPs remain static within one SISO snapshot. However over T MIMO snapshots, we only constrain the amplitudes of path weights remain the same, while their phases may experience variations captured by the Doppler shift and the switching schedule of antenna arrays.

Similar to the data model in [13] and [16], we use a vector model for the input T MIMO snapshots, and denote it as $\mathbf{y} \in \mathbb{C}^{M \times 1}$, where $M = M_f \times M_R \times M_T \times T$. It includes contributions from SP $\mathbf{s}(\boldsymbol{\theta}_s)$, DMC and measurement noise.

$$\mathbf{y} = \mathbf{s}(\boldsymbol{\theta}_s) + \mathbf{n}_{\text{dmc}} + \mathbf{n}_0, \tag{3}$$

where the vector $\boldsymbol{\theta}_s$ represents the parameters of P SPs. It consists of polarimetric path weights $\boldsymbol{\gamma}$ and the structural parameters $\boldsymbol{\mu}$ that include $\boldsymbol{\tau}$, $(\boldsymbol{\varphi}_T, \boldsymbol{\theta}_T)$, $(\boldsymbol{\varphi}_R, \boldsymbol{\theta}_R)$, and $\boldsymbol{\nu}$. $\boldsymbol{\varphi}_T$, $\boldsymbol{\varphi}_R$ and $\boldsymbol{\nu}$ are normalized to between $-\pi$ and π, $\boldsymbol{\theta}_T$ and $\boldsymbol{\theta}_R$ are between 0 and π, while $\boldsymbol{\tau}$ is normalized to between 0 and 2π.

Before breaking down the details about $\mathbf{s}(\boldsymbol{\theta}_s)$, we first introduce the phase shift matrix $\mathbf{A}(\boldsymbol{\mu}_i) \in \mathbb{C}^{M_i \times P}$ [13], which is given by

$$\mathbf{A}(\boldsymbol{\mu}_i) = \begin{bmatrix} e^{-j\lfloor \frac{M_i}{2} \rfloor \mu_{i,1}} & \cdots & e^{-j\lfloor \frac{M_i}{2} \rfloor \mu_{i,P}} \\ \vdots & & \vdots \\ e^{j\,(\lceil \frac{M_i}{2} \rceil - 1)\mu_{i,1}} & \cdots & e^{j\,(\lceil \frac{M_i}{2} \rceil - 1)\mu_{i,P}} \end{bmatrix}. \tag{4}$$

$\boldsymbol{\mu}_i$ is a structural parameter vector that represents either $\boldsymbol{\tau}$, $\boldsymbol{\varphi}_T$, $\boldsymbol{\theta}_T$, $\boldsymbol{\varphi}_R$, $\boldsymbol{\theta}_R$ or $\boldsymbol{\nu}$. Together with the system and array calibrations, such as the system frequency response $\mathbf{G}_f$ and the effective aperture distribution functions (EADFs) $\mathbf{G}_{TH}$, $\mathbf{G}_{TV}$, $\mathbf{G}_{RH}$, and $\mathbf{G}_{RV}$ introduced in [13] and [21], we obtain the basis matrices that form important pieces in our data model.

$$\mathbf{B}_f = \mathbf{G}_f \cdot \mathbf{A}(-\boldsymbol{\tau}) \tag{5}$$

$$\tilde{\mathbf{B}}_{TH} = \left[\mathbf{G}_{TH} \cdot \left(\mathbf{A}(\boldsymbol{\theta}_T) \diamond \mathbf{A}(\boldsymbol{\varphi}_T)\right)\right] \odot \mathbf{A}_{t,T}(\boldsymbol{\nu}) \tag{6}$$

$$\tilde{\mathbf{B}}_{TV} = \left[\mathbf{G}_{TV} \cdot \left(\mathbf{A}(\boldsymbol{\theta}_T) \diamond \mathbf{A}(\boldsymbol{\varphi}_T)\right)\right] \odot \mathbf{A}_{t,T}(\boldsymbol{\nu}) \tag{7}$$

$$\tilde{\mathbf{B}}_{RH} = \left[\mathbf{G}_{RH} \cdot \left(\mathbf{A}(\boldsymbol{\theta}_R) \diamond \mathbf{A}(\boldsymbol{\varphi}_R)\right)\right] \odot \mathbf{A}_{t,R}(\boldsymbol{\nu}) \tag{8}$$

$$\tilde{\mathbf{B}}_{RV} = \left[\mathbf{G}_{RV} \cdot \left(\mathbf{A}(\boldsymbol{\theta}_R) \diamond \mathbf{A}(\boldsymbol{\varphi}_R)\right)\right] \odot \mathbf{A}_{t,R}(\boldsymbol{\nu}) \tag{9}$$

$$\mathbf{B}_t = \mathbf{A}(\boldsymbol{\nu}) \tag{10}$$

Finally the signal data model for the responses of SPs is given by

$$\begin{aligned} \mathbf{s}(\boldsymbol{\theta}_s) = {} & \mathbf{B}_t \diamond \tilde{\mathbf{B}}_{TH} \diamond \tilde{\mathbf{B}}_{RH} \diamond \mathbf{B}_f \cdot \boldsymbol{\gamma}_{HH} \\ & + \mathbf{B}_t \diamond \tilde{\mathbf{B}}_{TH} \diamond \tilde{\mathbf{B}}_{RV} \diamond \mathbf{B}_f \cdot \boldsymbol{\gamma}_{HV} \\ & + \mathbf{B}_t \diamond \tilde{\mathbf{B}}_{TV} \diamond \tilde{\mathbf{B}}_{RH} \diamond \mathbf{B}_f \cdot \boldsymbol{\gamma}_{VH} \\ & + \mathbf{B}_t \diamond \tilde{\mathbf{B}}_{TV} \diamond \tilde{\mathbf{B}}_{RV} \diamond \mathbf{B}_f \cdot \boldsymbol{\gamma}_{VV}. \end{aligned} \tag{11}$$

Our model differs from the main model of [11] and [13] in that we *explicitly* include the Doppler shift as a parameter in the MIMO channel signal model, which is reflected in Eqs. (6)-(10). When the MIMO channel sounder uses the sequential switching scheme, $\mathbf{A}_{t,T}$ and $\mathbf{A}_{t,R}$ capture the phase rotation between measured sub-channels due to the Doppler shifts. This phase rotation becomes non-negligible when the Doppler shift or the time span is large. For example a path with the Doppler shift of 100Hz can create a phase difference of 720° over 20ms.

$$\mathbf{A}_{t,T}(\boldsymbol{\nu}) = \begin{bmatrix} e^{j\frac{t_{T,1}}{T_0}\nu_1} & \cdots & e^{j\frac{t_{T,1}}{T_0}\nu_P} \\ \vdots & \ddots & \vdots \\ e^{j\frac{t_{T,M_T}}{T_0}\nu_1} & \cdots & e^{j\frac{t_{T,M_T}}{T_0}\nu_P} \end{bmatrix} \tag{12}$$

$$\mathbf{A}_{t,R}(\boldsymbol{\nu}) = \begin{bmatrix} e^{j\frac{t_{R,1}}{T_0}\nu_1} & \cdots & e^{j\frac{t_{R,1}}{T_0}\nu_P} \\ \vdots & \ddots & \vdots \\ e^{j\frac{t_{R,M_R}}{T_0}\nu_1} & \cdots & e^{j\frac{t_{R,M_R}}{T_0}\nu_P} \end{bmatrix} \tag{13}$$

Here $t_{T,i}$ and $t_{R,j}$ are the starting time of the sub-channel measurement corresponding to ith Tx antenna and jth Rx antenna.

We also consider the influence of diffuse scattering in our measurements. It is well known electromagnetic waves are always partially scattered apart in addition to the specular reflection. Their total power may be non-negligible, even though each is weak. Besides, including DMC in the signal data model improves the robustness of the estimator [22]. We assume that DMC follows a zero-mean complex Gaussian process, and its covariance matrix has a Kronecker structure, which is given by

$$\mathbf{R}_{\text{dmc}} = \mathbf{I}_t \otimes \mathbf{R}_T \otimes \mathbf{R}_R \otimes \mathbf{R}_f. \tag{14}$$

This model allows us to characterize the correlation of the DMC process in the frequency and angular domains. Furthermore we assume that DMC and noise are independent, the covariance matrix of the stochastic part in the data model, i.e. $\mathbf{n}_{\text{dmc}} + \mathbf{n}_0$, is modeled by

$$\mathbf{R}_{\text{dan}} = \mathbf{R}_{\text{dmc}} + \sigma_n^2 \mathbf{I}. \tag{15}$$

We denote $\mathbf{R}_{\text{dan}}$ as $\mathbf{R}$ for brevity in the rest of paper.

III. Estimation Algorithm

We select the framework of RIMAX [13], because it provides an MLE that is both robust and efficient. RIMAX implements a *joint* optimization of all parameters of SPs and it converges considerably faster compared to the SAGE algorithm used in [11] to analyze the V2V channel measurement data. Besides, RIMAX includes DMC as a part of the stochastic components in the channel response, which provides a complete data model and produces stable estimates. We first review some key points about the framework of RIMAX, and then focus on the efficient implementation of parameter initialization and optimization for SPs regarding with our new data model discussed in Section II.

The general expression of the MLE with the observation vector $\mathbf{y}$ and parameters $\boldsymbol{\theta}$ is given by

$$\hat{\boldsymbol{\theta}} = \underset{\boldsymbol{\theta}}{\text{argmax}} \big\{ \mathcal{P}_r(\mathbf{y}, \boldsymbol{\theta}) \big\}. \tag{16}$$

In the application of wireless channel sounding, we typically assume that we have no prior information about $\boldsymbol{\theta}$. We can also separate $\boldsymbol{\theta}$ into $\boldsymbol{\theta}_s$ for SPs and $\boldsymbol{\theta}_d$ for DMC to arrive at

$$\begin{bmatrix} \hat{\boldsymbol{\theta}}_s \\ \hat{\boldsymbol{\theta}}_d \end{bmatrix} = \underset{\boldsymbol{\theta}}{\text{argmax}} \{ \mathcal{P}_r(\mathbf{y}|\boldsymbol{\theta}) \}. \tag{17}$$

Given the system model in Eq. (3), the distribution of $\mathbf{y}$ is $\mathcal{CN}(\mathbf{s}(\boldsymbol{\theta}_s), \mathbf{R})$, and the conditional probability is determined by

$$\mathcal{P}_r(\mathbf{y}|\boldsymbol{\theta}) = \frac{1}{\pi^M \det(\mathbf{R})} e^{-[\mathbf{y}-\mathbf{s}(\boldsymbol{\theta}_s)]^\dagger \mathbf{R}^{-1} [\mathbf{y}-\mathbf{s}(\boldsymbol{\theta}_s)]}. \tag{18}$$

There is no closed-form solution of Eq. (17), because $\mathbf{s}(\boldsymbol{\theta}_s)$ is a highly nonlinear function of $\boldsymbol{\mu}$ in $\boldsymbol{\theta}_s$. RIMAX updates $\boldsymbol{\theta}_s$ and $\boldsymbol{\theta}_d$ separately and iteratively. With a fixed estimate of $\mathbf{R}$, RIMAX improves $\boldsymbol{\theta}_s$ with the Levenberg-Marquardt (LM) method [14], [15]. Its input is an initial value of $\boldsymbol{\theta}_s$, which we obtain either from the global initialization algorithm or from the previous snapshot. The main update equation of $\boldsymbol{\theta}_s$ within the LM method is given by

$$\hat{\boldsymbol{\theta}}_s^{i+1} = \hat{\boldsymbol{\theta}}_s^{i} + \big[\mathcal{J}(\hat{\boldsymbol{\theta}}_s^{i}, \mathbf{R}) + \zeta \mathbf{I} \odot \mathcal{J}(\hat{\boldsymbol{\theta}}_s^{i}, \mathbf{R}) \big]^{-1} \mathbf{q}(\mathbf{y}|\hat{\boldsymbol{\theta}}_s^{i}, \mathbf{R}). \tag{19}$$

Here ζ is the parameter to control the update step size. This iterative optimization step requires the evaluation of the score function $\mathbf{q}(\mathbf{y}|\boldsymbol{\theta}_s, \mathbf{R})$ and FIM $\mathcal{J}(\boldsymbol{\theta}_s, \mathbf{R})$, for which we will provide more details later in this section.

This paper mainly focuses on the method to estimate $\boldsymbol{\theta}_s$. $\boldsymbol{\theta}_d$ is estimated based on [13, Tables 6-5 and 6-6] for a simplified DMC model that is explained in Section III-A, while [23] introduces an MLE for the general model described in Eqs. (14) and (15).

As a summary, our proposed algorithm performs a joint parameter estimation for SPs and DMC in the V2V channels. Fig. 2 gives a flowchart of the algorithm. There are two main differences when we compare it to the original RIMAX scheme in [13]. The first difference is the increased complexity of the signal data model of SPs due to the inclusion of phase shift between antennas, which is necessary for time-varying V2V channels, but we manage to accommodate it with optimized numerical implementations. The second difference is that we place the detection on new paths at the end of the snapshot instead of at the beginning, because for a typical fast time-varying V2V channel it is preferable to further polish the entire parameter vector $\boldsymbol{\theta}_s$ before evaluating the residual response $\mathbf{y} - \mathbf{s}(\boldsymbol{\theta}_s)$ and detecting the new paths. Our scheme has shown an overall better stability of the estimates of SPs and reasonable values of the diffuse power ratio (dPR), which is illustrated by the evaluation results in Section IV-B.

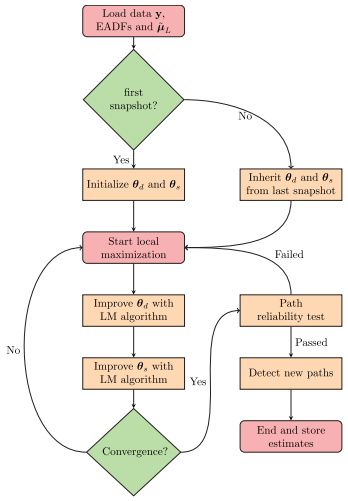

Fig. 2. The flowchart of the HRPE scheme to evaluate V2V MIMO channel measurements.

A. Reduced Data Model

In this section we describe a simplified data model that suits our measurement setup, which is described with details in [20]. The simplified model focuses on the vertical-to-vertical polarization component, because both Tx and Rx deploy vertically polarized antenna arrays. Besides, the angular

modeling is limited to the azimuthal domain because the 8-element uniform circular array (UCA) has an ambiguity in the elevation domain. It is assumed that these assumptions do not significantly deteriorate the estimation in the V2V application, especially when the height difference between two arrays mounted on top of the vehicles is small. In Sec. IV-B, the diffuse power ratio (dPR) and the generally good agreements between the extracted SPs with the environment indicate that the above-mentioned assumptions may be justified in our measured scenarios. However these assumptions don't hold in general for all channel sounding applications, see [22]. The reduced data model of the response of SPs is then given by

$$\mathbf{s}(\boldsymbol{\theta}_s) = \mathbf{B}_t \diamond \tilde{\mathbf{B}}_{TV} \diamond \tilde{\mathbf{B}}_{RV} \diamond \mathbf{B}_f \cdot \boldsymbol{\gamma}_{VV}, \tag{20}$$

where $\boldsymbol{\theta}_s = [\boldsymbol{\mu}, \boldsymbol{\gamma}_{VV}]$.

We have also selected a simplified DMC model that originates from [24]. The model assumes the DMC process is only correlated in frequency, and its power delay profile (PDP) follows a single exponential decay model. The main reason is that the entire estimator with the simplified DMC model produces more stable results over a continuous route of measurement points. As a result, the covariance matrix $\mathbf{R}_{\text{dmc}}$ from Eq. (14) is reduced to

$$\mathbf{R}_{\text{dmc}} = \mathbf{I}_t \otimes \mathbf{I}_T \otimes \mathbf{I}_R \otimes \mathbf{R}_f \tag{21}$$

$$\mathbf{R}_\tau = \mathbf{F}^\dagger \mathbf{R}_f \mathbf{F}, \tag{22}$$

where $\mathbf{F}$ is the discrete Fourier transform (DFT) matrix and $\mathbf{R}_\tau$ is a diagonal matrix.

B. Initialization Method

Accurate initial estimates of the parameters improve the estimation performance for most MLEs that implement a local optimization algorithm. Our initialization algorithm is applied to the beginning of the first snapshot, as well as to the end of each snapshot to detect new paths. Therefore it forms an essential part of the whole estimator, and could dominate the overall complexity of the algorithm if an inferior method is used. To initialize the parameters of one SP, a global search on a multi-dimensional parameter grid can be computationally expensive. Therefore [13] and [25] avoid the global search on the large grid and resort to a sequential search in separate dimensions. The method reduces the computational efforts, but it sarcrifices the correlation gain of a joint multi-dimensional search, which can lead to inaccurate initial estimates or a misdetection of weak SPs. In this part, we propose an efficient initialization method for the parameters of SPs, which exploits the full correlation gain and has a significantly reduced runtime. The new method is an extension of what we introduced in our conference paper [18].

Although the model has a new data dimension (the time domain) in Eqs. (11) and (20), the same correlation function for a single SP with structural parameters $\boldsymbol{\mu}$ in [18] can still be applied.

$$C(\boldsymbol{\mu}, \mathbf{y}) = (\mathbf{y}^\dagger \mathbf{R}^{-1} \mathbf{B})(\mathbf{B}^\dagger \mathbf{R}^{-1} \mathbf{B})^{-1} (\mathbf{B}^\dagger \mathbf{R}^{-1} \mathbf{y}). \tag{23}$$

Reference [13] proves that locating peaks of the correlation function in Eq. (23) is indeed closely related to solving the MLE, given an initial estimate of $\mathbf{R}$. However there is no closed-form solution to locate these correlation peaks. Our method sequentially detects, estimates and substracts SPs in a descending order of their SNRs. It continues until the maximal correlation value $C_{\max}$ falls below a certain threshold ϵ_D[1] or the number of detected paths has exceeded a limit. The pseudocode for the initialization part is similar to that in [18] and provided in Algorithm 1.

Algorithm 1 Algorithm for Initializing Parameters of SPs

```
Load y and the large search grid μ̃_L;
μ = []; y_res = y;
Compute C(μ̃_L, y_res), and find its peak C_max and μ_max;
while C_max ≥ ε_D and need more SPs do
  while stopzoom == 0 do
    Construct a small grid μ̃_s around μ_max;
    Compute C(μ̃_s, y_res), and update μ_max;
    if All changes are small then
      stopzoom = 1;
    else
      stopzoom = 0;
    end if
  end while
  μ = [μ; μ_max]; Compute γ_VV from Eq. (24);
  Construct θ_s = [μ; γ_VV]; y_res = y − s(θ_s);
  Compute C(μ̃_L, y_res), and find its peak C_max and μ_max;
end while
```

Given the observation vector $\mathbf{y}$ and structural parameters $\boldsymbol{\mu}$, the best linear unbiased estimator (BLUE) of $\boldsymbol{\gamma}_{VV}$ for the data model in Eq. (20) is

$$\hat{\boldsymbol{\gamma}}_{VV} = (\mathbf{B}^\dagger \mathbf{R}^{-1} \mathbf{B})^{-1} \mathbf{B}^\dagger \mathbf{R}^{-1} \mathbf{y} \tag{24}$$

A 4-dimensional (4D) search grid $\tilde{\mu}_L$ is needed for the initial path detection. A rule of thumb for sufficient oversampling in every parameter domain is that $N_f = 2M_f$, $N_T = 2M_T$, $N_R = 2M_R$ and $N_t = 2T$ [16]. Similar to the approach in our previous work [18], our method exploits the data structure of $\mathbf{y}$ and uses tensor products to greatly accelerate the computation [26]. Let us introduce the 4D correlation tensor $\mathcal{C}$ that shares the same dimension with $\tilde{\mu}$. With a given Doppler shift ν_{n_t} (n_tth Doppler point), we then introduce two 3-dimensional (3D) tensors $\mathcal{T}_1^{n_t}$ and $\mathcal{T}_2^{n_t}$ that have the dimension of $N_f \times N_R \times N_T$. We can compute the n_tth 3D child tensor of $\mathcal{C}$ as

$$\mathcal{C}(:, :, :, n_t) = \left|\mathcal{T}_1^{n_t}\right|^2 \oslash \mathcal{T}_2^{n_t}, \tag{25}$$

where $||^2$ is the element-wise absolute square, and $\oslash$ is the element-wise division between two tensors. Appendix A reveals the detailed procedures on how to compute the two tensors $\mathcal{T}_1^{n_t}$ and $\mathcal{T}_2^{n_t}$.

C. Score Function and FIM

The score function and FIM are important elements in the nonlinear optimization solution given by Eq. (19). The score

[1] An empirical value of 100 is chosen for evaluating the V2V measurement data in Sec. IV-B.

function is known as the first order partial derivative of the log-likelihood function, which is given by

$$\mathbf{q}(\mathbf{y}|\boldsymbol{\theta}_s, \mathbf{R}) = \frac{\partial}{\partial \boldsymbol{\theta}_s} \ln(\mathcal{P}_r(\mathbf{y}|\boldsymbol{\theta})) \tag{26}$$

$$= 2\mathcal{R}\{\mathbf{D}^{\dagger}(\boldsymbol{\theta}_s)\mathbf{R}^{-1}(\mathbf{y} - \mathbf{s}(\boldsymbol{\theta}_s))\}, \tag{27}$$

where $\mathcal{R}\{\}$ takes the real value of the expression. On the other hand the FIM is the negative covariance matrix of the score function, which is defined as

$$\mathbf{J}(\boldsymbol{\theta}_s, \mathbf{R}) = 2\mathcal{R}\big\{\mathbf{D}(\boldsymbol{\theta}_s)^{\dagger}\mathbf{R}^{-1}\mathbf{D}(\boldsymbol{\theta}_s)\big\}. \tag{28}$$

Both the score function and FIM require the value of the Jacobian matrix $\mathbf{D}(\boldsymbol{\theta}_s)$, which is defined as

$$\mathbf{D}(\boldsymbol{\theta}_s) = \frac{\partial}{\partial \boldsymbol{\theta}_s}\mathbf{s}(\boldsymbol{\theta}_s) \in \mathbb{C}^{M\times L}. \tag{29}$$

Here $L = 6P$ is the length of $\boldsymbol{\theta}_s$, i.e. the total number of parameters related with P SPs. As suggested in [13] and [16], it is not feasible to directly evaluate the score function in Eq. (27) or the inverse of FIM in Eq. (28), mainly because of the large measurement dimension M. Our method utilizes the special structure of the problem to speed up the computation. The key to our method is that we may reorganize the Jacobian matrix $\mathbf{D}(\boldsymbol{\theta}_s)$ as a sum of Khatri-Rao products of four matrices.

$$\mathbf{D}(\boldsymbol{\theta}_s) = \frac{1}{3}\big(\mathbf{D}_4^1 \diamond \mathbf{D}_3^1 \diamond \mathbf{D}_2^1 \diamond \mathbf{D}_1 + \mathbf{D}_4^1 \diamond \mathbf{D}_3^2 \diamond \mathbf{D}_2^2 \diamond \mathbf{D}_1 + \mathbf{D}_4^2 \diamond \mathbf{D}_3^2 \diamond \mathbf{D}_2^1 \diamond \mathbf{D}_1\big) \tag{30}$$

$$= \frac{1}{3}(\mathbf{D}1 + \mathbf{D}2 + \mathbf{D}3), \tag{31}$$

The detailed structures of all these $\mathbf{D}_i^j$ matrices are given in Tab. III. To reconstruct a $\mathbf{D}_i^j$ with the table, one can concatenate the sub-matrices related to $\mathbf{D}_i^j$ along the row direction. Each element in the table has P columns, where P is the number of SPs.

With the new expression of the Jacobian matrix $\mathbf{D}(\boldsymbol{\theta}_s)$, the score function from Eq. (27) becomes

$$\mathbf{q}(\mathbf{y}|\boldsymbol{\theta}_s, \mathbf{R}) = \frac{2}{3}\mathcal{R}\big\{(\mathbf{D}1 + \mathbf{D}2 + \mathbf{D}3)^{\dagger}\mathbf{R}^{-1}(\mathbf{y} - \mathbf{s}(\boldsymbol{\theta}_s))\big\}, \tag{32}$$

which consists of three small similar terms. In the following we show results for $\mathbf{D}1^{\dagger}\mathbf{R}^{-1}(\mathbf{y} - \mathbf{s}(\boldsymbol{\theta}_s))$, and the other terms behave similarly. If we use the eigenvalue decomposition of $\mathbf{R}$ in Eqs. (52)-(54), the small term becomes

$$\mathbf{D}1^{\dagger}\mathbf{R}^{-1}(\mathbf{y} - \mathbf{s}(\boldsymbol{\theta}_s)) = \mathbf{D}1^{\dagger}\mathbf{U}\boldsymbol{\Lambda}^{-1}\mathbf{U}^{\dagger}(\mathbf{y} - \mathbf{s}(\boldsymbol{\theta}_s)) \tag{33}$$

$$= \mathbf{D}1'^{\dagger}\boldsymbol{\Lambda}^{-1}\mathbf{U}^{\dagger}(\mathbf{y} - \mathbf{s}(\boldsymbol{\theta}_s)) \tag{34}$$

$$= \mathbf{D}1'^{\dagger}\mathbf{y}'_{\text{res}} \tag{35}$$

where the projected matrix $\mathbf{D}1'$ is defined as

$$\mathbf{D}1' = \mathbf{U}^{\dagger}\mathbf{D}1 \tag{36}$$

$$= (\mathbf{I}_t \otimes \mathbf{U}_T \otimes \mathbf{U}_R \otimes \mathbf{U}_f)^{\dagger}\mathbf{D}1 \tag{37}$$

$$= (\mathbf{I}_t\mathbf{D}_4^1) \diamond (\mathbf{U}_T^{\dagger}\mathbf{D}_3^1) \diamond (\mathbf{U}_R^{\dagger}\mathbf{D}_2^1) \diamond (\mathbf{U}_f^{\dagger}\mathbf{D}_1) \tag{38}$$

$$= \mathbf{D}_4^{1\prime} \diamond \mathbf{D}_3^{1\prime} \diamond \mathbf{D}_2^{1\prime} \diamond \mathbf{D}'_1. \tag{39}$$

An efficient method to compute $\mathbf{y}'_{\text{res}}$ is provided in Eq. (58) through tensor operations. As a result, we can follow the numerical method summarized in [13, Table 5-4] to compute Eq. (35).

To find an alternative expression for the FIM, we substitute Eq. (31) into Eq. (28) and have

$$\mathbf{J} = \frac{2}{9}\mathcal{R}\big\{(\mathbf{D}1 + \mathbf{D}2 + \mathbf{D}3)^{\dagger}\mathbf{R}^{-1}(\mathbf{D}1 + \mathbf{D}2 + \mathbf{D}3)\big\} \tag{40}$$

$$= \frac{2}{9}\mathcal{R}\big\{\sum_{i=1}^{3}\sum_{j=1}^{3}\mathbf{D}i^{\dagger}\mathbf{R}^{-1}\mathbf{D}j\big\}. \tag{41}$$

Here we have 9 elements that follow the structure $\mathbf{D}ij = \mathbf{D}i^{\dagger}\mathbf{R}^{-1}\mathbf{D}j$, and $\mathbf{D}ji = \mathbf{D}ij^{\dagger}$. We can evaluate each of them following the approach similar to [27, eq. (42)]. For instance, with an eigenvalue decomposition on $\mathbf{R}$ we can rewrite $\mathbf{D}12$ as

$$\mathbf{D}12 = \mathbf{D}1^{\dagger}\mathbf{R}^{-1}\mathbf{D}2 \tag{42}$$

$$= \mathbf{D}1^{\dagger}\mathbf{U}\boldsymbol{\Lambda}^{-1}\mathbf{U}^{\dagger}\mathbf{D}2 \tag{43}$$

$$= \mathbf{D}1'^{\dagger}\boldsymbol{\Lambda}^{-1}\mathbf{D}2'. \tag{44}$$

Similar to the definition of $\mathbf{D}1'$ in Eq. (39), $\mathbf{D}2'$ is given by

$$\mathbf{D}2' = \mathbf{U}^{\dagger}\mathbf{D}2 \tag{45}$$

$$= \mathbf{D}_4^{1\prime} \diamond \mathbf{D}_3^{2\prime} \diamond \mathbf{D}_2^{2\prime} \diamond \mathbf{D}'_1. \tag{46}$$

Next according to the PARATREE model proposed in [27], we may decompose a 4D tensor reshaped from the diagonal vector of $\boldsymbol{\Lambda}^{-1}$, then find an approximate expression for $\boldsymbol{\Lambda}^{-1}$ given by

$$\boldsymbol{\Lambda}^{-1} \approx \sum_{r_f}\sum_{r_R}\sum_{r_T} \boldsymbol{\Lambda}^{(t)}_{r_f,r_R,r_T} \otimes \boldsymbol{\Lambda}^{(T)}_{r_f,r_R,r_T} \otimes \boldsymbol{\Lambda}^{(R)}_{r_f,r_R} \otimes \boldsymbol{\Lambda}^{(f)}_{r_f}. \tag{47}$$

Appendix B provides more details on this approximation expression. After combining Eqs. (39), (46), and (47) into Eq. (44), we finally arrive at an approximate and simpler expression to evaluate $\mathbf{D}12$.

$$\mathbf{D}12 \approx \sum_{r_f}(\mathbf{D}_1'^{\dagger}\boldsymbol{\Lambda}^{(f)}_{r_f}\mathbf{D}'_1) \odot \sum_{r_R}(\mathbf{D}_2^{1\prime\dagger}\boldsymbol{\Lambda}^{(R)}_{r_f,r_R}\mathbf{D}_2^{2\prime}) \odot \sum_{r_T}(\mathbf{D}_3^{1\prime\dagger}\boldsymbol{\Lambda}^{(T)}_{r_f,r_R,r_T}\mathbf{D}_3^{2\prime}) \odot (\mathbf{D}_4^{1\prime\dagger}\boldsymbol{\Lambda}^{(t)}_{r_f,r_R,r_T}\mathbf{D}_4^{1\prime}) \tag{48}$$

The other eight elements in Eq. (41) can also use this method to speed up the evaluation.

IV. Validation

A. Simulation

We have conducted some simulations based on synthetic two-path channel responses from Eq. (1), where we assume there are only two SPs affected by white measurement noise. The simulations don't consider the effect of DMC, because our method shares the same DMC estimator with that in [13]. With the knowledge of the true parameters, we can compare root mean square errors (RMSEs) of estimates between two estimators. The first is our method, and the second one is the main method in [13] which neglects the phase variation between antenna switching within one MIMO snapshot.

(a) A black SUV passes by Rx

(b) Rx approaches Tx

(c) Tx turns around the corner

Fig. 3. The screenshots of the video taken from the 360° camera at the Rx SUV. (a) A black SUV passes by Rx. (b) Rx approaches Tx. (c) Tx turns around the corner.

TABLE I

RMSE COMPARISON BASED ON SYNTHETIC TWO PATH CHANNEL WITH ONE LOW AND ONE HIGH DOPPLER SHIFT (10,400) Hz, OUR ESIMATOR / [13]

	Path 1		Path 2	
	True	RMSE	True	RMSE
τ(ns)	1835.4	1.55e-02/1.55e-02	1100.9	5.93e-02/5.90e-02
φ_T(deg)	-94.8	1.14e-02/1.17e-01	-42.3	4.35e-02/4.83
φ_R(deg)	2.3	1.10e-02/1.31e-02	178.3	6.46e-02/4.49e-01
ν(Hz)	10.0	1.20e-02/1.20e-02	400.0	5.53e-02/5.54e-02
$\lvert\gamma\rvert^2$(dB)	-6.3	3.07e-03/3.03e-03	-18.7	1.51e-02/8.28e-02

The simulation results are listed in Tab. I. We can observe that the RMSEs from the two estimators are similar, except for φ_T, φ_R and $|\gamma|^2$ where our method almost always presents the smallest RMSE. The second estimator gives a high RMSE for φ_T and φ_R whenever the Doppler shift is *not small*. The reason of large RMSE for angular estimates in the second estimator is that it neglects the phase variation between antenna switching. Its RMSE of φ_T is higher than that of φ_R when the Doppler shift is large, as illustrated by Path 2 in Tab. I. This effect results from the switching pattern applied in this work, as shown in Fig. 1 that the phase offset will be larger between adjacent Tx antenna switching than Rx due to the bigger time gap. Therefore in the second estimator, neglecting the phase variation between antenna switching has a worse impact on φ_T than φ_R.

B. Measurement

In this section, we apply our HRPE algorithm to the V2V measurement data collected by a real-time MIMO channel sounder that we have constructed. The sounder includes a pair of NI-USRP RIOs as the main RF transceivers, two GPS-disciplined rubidium references as the synchronization units and a pair of 8-element UCAs. The design of our channel sounder focuses on the system stability and the real-time streaming capability. With careful system and array calibrations, the setup allows us to analyze the measurement data with our HRPE algorithm. The increased measurement snapshot rate expands the resolvable range of Doppler shift to $\pm$806 Hz without ambiguities, meanwhile the increased number of samples provides a smoother picture of the evolution of parameters of SPs. Tab II presents the key parameters of the setup. More details can be found in [20].

TABLE II

PARAMETERS OF THE REAL-TIME V2V MIMO CHANNEL SOUNDER

Parameter	Value
Carrier frequency	5.9 GHz
Bandwidth	15 MHz
Transmit power	26 dBm
Sampling rate	20 MS/s
Length of the sounding signal $\tau_{\max}$	4 μs
MIMO signal duration T_0	620 μs
Number of frequency tones M_f	61
Number of Tx antennas M_T	8
Number of Rx antennas M_R	8
Number of MIMO per burst T	30
Rate of bursts	20 Hz

Fig. 3 provides three screenshots of the video taken by the 360° camera mounted on top of the Rx array. Fig. 4 presents the route and map of the sample measurements.

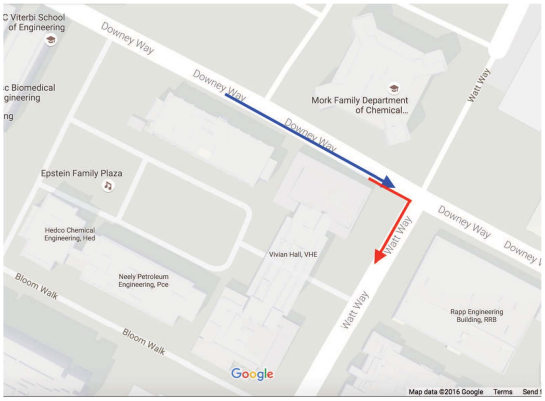

Fig. 4. The route and map of the V2V measurements on USC campus, near the GPS location of (34° 1′ 13.08" N, 118° 17′ 16.80" W), where the blue arrow is the route of the Rx vehicle, and the red arrow is the route of the Tx vehicle.

We split this continuous measurement route into four parts. Some sample average power delay profiles (APDPs) are presented in Fig. 6, where "Data" is the APDP of $\mathbf{y}$, "SP" is $\mathbf{s}(\hat{\boldsymbol{\theta}}_s)$, "Res" is $\mathbf{y} - \mathbf{s}(\hat{\boldsymbol{\theta}}_s)$ and "DMC" is the diagonal of $\mathbf{R}_\tau$. The Tx and Rx vehicles start with static positions. A sample APDP for this scenario is shown in Fig. 6(a). We define the driving direction of the vehicle as 0° in azimuth. As shown in Fig. 3, the red Tx SUV is in front of the Rx SUV and facing away. The angular power spectrum (APS) between 10 s and 30 s in Fig. 7(d) verifies the azimuth DoA of the strong MPCs. Meanwhile the Rx vehicle is in the azimuth direction of 180°, or equivalently −180°, from the perspective of the Tx vehicle, and the results between 10 s and 30 s in Fig. 7(c) verify the azimuth DoD of dominant MPCs.

In the second scenario, a third black SUV passes the Rx SUV from behind to its front, stops behind the Tx SUV for a while, and partially blocks the line-of-sight (LOS), as shown in Fig. 3(a). A sample APDP for this scenario is given in Fig. 6(b). When compared to Fig. 6(a), it shows the blockage by the third SUV results in an approximate 5 dB attenuation of the received power. A string of dots with a high Doppler shift between $t = 10$ s and 20 s in Fig. 7(b) corresponds to the MPCs from the passing black SUV. The Doppler shift quickly falls to zero when the third SUV moves into the space between the Tx and Rx SUVs, which also explains the waterfall shape of the string of dots.

In the third scenario, the black SUV changes lane and passes the Tx around $t = 40$ s, which explains a string of dots with large negative Doppler between $t = 40$ s and 45 s in Fig. 7(b). Meanwhile around $t = 45$ s, the Rx car pulls out from the right curb into the middle of the road. This subtle swing of the driving direction is also tracked and reflected by the results around 40 s in Fig. 7(d), when the direction of dominant SPs evolves from 0° to approximately −30° and back to 0°. The Rx car starts moving towards the Tx, when the Tx car remains static until the Rx car almost reaches the rear of the Tx around 60 s. Results between 40 s and 60 s in Figs. 7(a) and 7(b) match this activity with decreased delays, positive Doppler shifts and increased power of the dominant SPs.

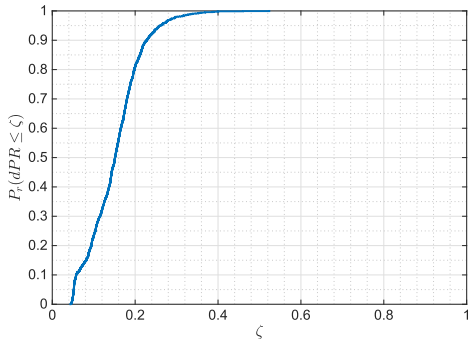

Fig. 5. The CDF of the dPR based on 1400 snapshots from the continuous V2V measurement on USC campus.

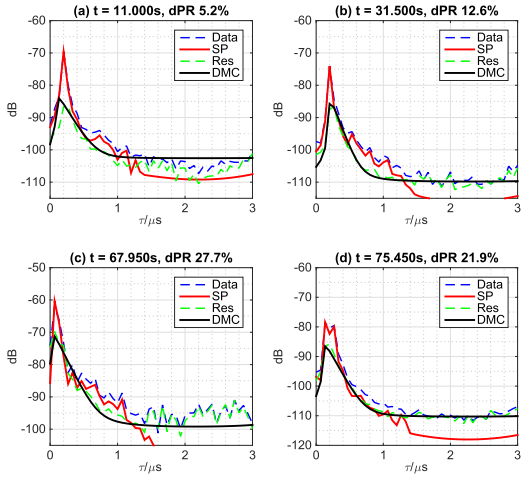

Fig. 6. Sample APDPs of (a) scenario I: Tx and Rx are both static with LOS (b) scenario II: Tx and Rx are both static with LOS obstructed a third SUV (c) scenario III: Rx drives toward Tx with LOS (d) scenario IV: Tx drives around the corner with LOS obstructed by the building.

In the fourth scenario, the Rx stops behind the stop sign, while the Tx SUV starts turning right at the corner around $t = 60$ s before disappearing from the sight of Rx at the intersection around $t = 70$ s. Fig. 3(c) provides a picture of this scenario. The scatter plot in Fig. 7(a) indicates an increase of the delays of strong SPs during this period, while Fig. 7(b) shows that the strong SPs have negative Doppler shifts, because the distance between Tx and Rx increases. The azimuth DoA and DoD of the strong SPs also evolve during this process, as shown in Figs. 7(c) and 7(d). Fig. 6(c) gives a sample APDP for this scenario. Between $t = 70$ s and $t = 80$ s the link between Tx and Rx is fully obstructed by the the building. Figs. 7(c) and 7(d) provide the angles of the main SPs in this NLOS scenario and indicate they are mostly likely the diffraction around the corner and the reflection from the wall of the building. Fig. 6(d) gives a sample APDP for this NLOS scenario.

To evaluate the performance of the estimator and the goodness-of-fit of the model, we examine the dPR, and it is the power ratio due to the contribution of DMC.

$$\text{dPR} = \frac{\|\mathbf{y} - \mathbf{s}(\hat{\boldsymbol{\theta}}_s)\|^2 - M\sigma_n^2}{\|\mathbf{y}\|^2}. \tag{49}$$

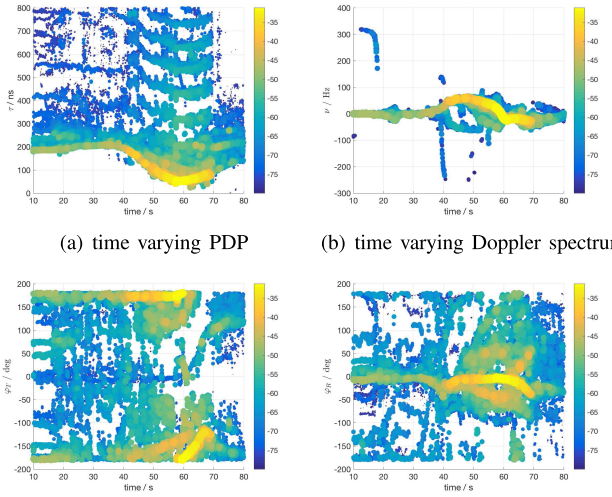

(a) time varying PDP (b) time varying Doppler spectrum

(c) time varying APS at Tx (d) time varying APS at Rx

Fig. 7. Color weighted scattered plots of extracted SPs, we show the SPs whose $|\gamma_{VV}|^2$ are greater then -80 dB. (a) Time varying PDP. (b) Time varying Doppler spectrum. (c) Time varying APS at Tx. (d) Time varying APS at Rx.

Fig. 5 gives the CDF of dPR from the evaluation of 1400 MIMO burst snapshots on this route, and indicates about 80% of the path extraction results have a dPR less than 0.2. The values of dPR are comparable to the ones in [28]–[30]. It is noteworthy that the average dPR is higher when the distance between Tx and Rx is less than 20m. An example of such case is given in Fig. 6(c). We conjecture it is because the modeling mismatch gets worse at a shorter distance between Tx and Rx, because of the assumption that SPs travel in the horizontal plane and the data model may omit the elevation angles. However the performance of the estimator is satisfying because most of the dominant SPs can be traced and mapped to the environment. Another plausible interpretation is that the number of scatterers illuminated by the Tx increases when the distance is small, which leads to a relatively larger dPR.

From the extracted SPs we can conveniently compute some important channel metrics such as root mean square (RMS) delay spread, Doppler spread and angular spread. Figs. 8(a) and 8(b) present the RMS delay and Doppler spread based on the extracted SPs. They are basically the square root of the second central moment of the power delay profile and Doppler spectrum. Both the delay spread and Doppler spread are important channel metrics in 802.11p [31]. Meanwhile Figs. 9(a) and 9(b) show the angular spread σ_φ for DoD and DoA, which is computed by

$$\mu_\varphi = \frac{\sum_{p=1}^{P} e^{j\varphi_p}|\gamma_{VV,p}|^2}{\sum_{p=1}^{P}|\gamma_{VV,p}|^2} \tag{50}$$

$$\sigma_\varphi = \sqrt{\frac{\sum_{p=1}^{P}|e^{j\varphi_p}-\mu_\varphi|^2|\gamma_{VV,p}|^2}{\sum_{p=1}^{P}|\gamma_{VV,p}|^2}}. \tag{51}$$

We observe in Fig. 9(a) that the angular spread of DoD increases in the second and fourth scenarios when the LOS is obstructed, while it decreases in the third scenario when

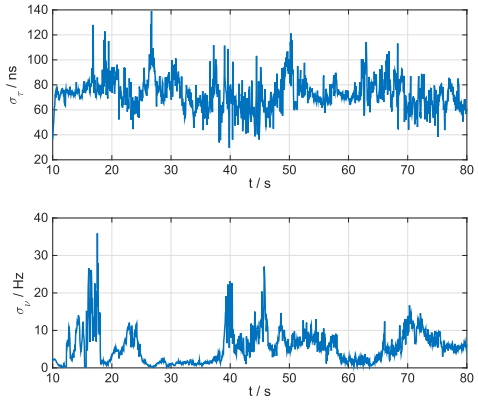

Fig. 8. The time-varying RMS delay and Doppler spread of SPs from the sample continuous route.

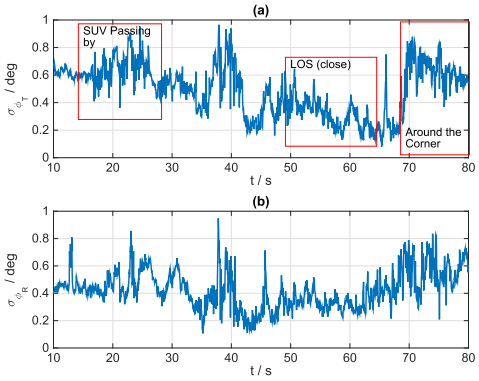

Fig. 9. The time-varying angular spread of (a) azimuth DoD, (b) azimuth DoA.

a strong LOS is present. A smart antenna system can exploit some multiplexing gain in the second and fourth scenarios and some beamforming gain in the third one.

V. Conclusion

In this paper we introduced a robust and efficient HRPE algorithm to evaluate the time-varying V2V channel. The new scheme provides a joint estimation of the delay, DoD, DoA and Doppler shift of MPCs with a high accuracy. We have also optimized the numerical implementation of the algorithm to allow a fast evaluation for large number of points on a continuous measurement route. We have validated our estimation scheme with actual V2V channel measurement data. Results have indicated an overall good performance of the estimator, which is based on the reasonable values of dPR and the observation that strong SPs match well with the environment and the dynamics of the measurement. These new results will enable a deeper insight into the propagation mechanism of the V2V channel and provide the necessary tools to develop a new or better V2V channel model.

Appendix A
Computation of 3D Tensors $\mathcal{T}_1$ and $\mathcal{T}_2$

The two 3D tensors $\mathcal{T}_1$ and $\mathcal{T}_2$ are important elements in computing the correlation grid in Eq. (25). First we introduce

their relationship with the correlation function defined in Eq. (23). We assume that an estimator has provided the eigenvalues and eigenvectors of the covariance matrix $\mathbf{R}$ for DMC and measurement noise, which follows the data model in Eqs. (14) and (15).

$$\mathbf{R} = \mathbf{U}\mathbf{\Lambda}\mathbf{U}^{\dagger} \tag{52}$$
$$\mathbf{U} = \mathbf{I}_t \otimes \mathbf{U}_T \otimes \mathbf{U}_R \otimes \mathbf{U}_f \tag{53}$$
$$\mathbf{\Lambda} = \mathbf{I}_t \otimes \mathbf{\Lambda}_T \otimes \mathbf{\Lambda}_R \otimes \mathbf{\Lambda}_f + \sigma_n^2\mathbf{I} \tag{54}$$

By utilizing $\mathbf{U}$ and $\mathbf{\Lambda}$ we can pre-process the observation vector $\mathbf{y}$ and the basis matrix $\mathbf{B}$,

$$\mathbf{y}' = \mathbf{\Lambda}^{-1}\mathbf{U}^{\dagger}\mathbf{y} \tag{55}$$
$$\mathbf{B}'(\boldsymbol{\mu}) = \mathbf{U}^{\dagger}\mathbf{B}(\boldsymbol{\mu}). \tag{56}$$

An efficient implementation of Eq. (55) is through tensor operations, which is given by

$$\mathcal{Y} = \text{reshape}\big(\mathbf{y}, [M_f \ M_R \ M_T \ T]\big) \tag{57}$$
$$\mathbf{y}' = \text{vec}\left\{\left[\left((\mathcal{Y} \times_1 \mathbf{U}_f^{\dagger}) \times_2 \mathbf{U}_R^{\dagger}\right) \times_3 \mathbf{U}_T^{\dagger}\right] \times_4 \mathbf{I}_t\right\} \oslash \boldsymbol{\lambda}. \tag{58}$$

Here "reshape()" and "vec()" are standard MATLAB commands to transform between a vector and a tensor. $\boldsymbol{\lambda}$ is the diagonal vector of $\mathbf{\Lambda}$. The $\times_n$ represents the n-mode product between a matrix and a tensor [32]. Similarly we may form a 4D data tensor $\mathcal{Y}'$ from $\mathbf{y}'$ according to Eq. (57).

After substituting Eqs. (55) and (56) into Eq. (23), we have an alternative expression for the correlation function

$$C(\boldsymbol{\mu}, \mathbf{y}') = (\mathbf{y}'^{\dagger}\mathbf{B}')(\mathbf{B}'^{\dagger}\mathbf{\Lambda}^{-1}\mathbf{B}')^{-1}(\mathbf{B}'^{\dagger}\mathbf{y}') \tag{59}$$

Each point on the large search grid $\tilde{\boldsymbol{\mu}}_L$ represents the structural parameters for one potential SP. The correlation grid $\mathcal{C}$, based on Eq. (59) and $\tilde{\boldsymbol{\mu}}_L$, has the same dimension with $\tilde{\boldsymbol{\mu}}_L$. From Eq. (59), we may observe that the 4D tensors $\mathcal{T}_1$ and $\mathcal{T}_2$ correspond to the two terms $\mathbf{B}'^{\dagger}\mathbf{y}'$ and $\mathbf{B}'^{\dagger}\mathbf{\Lambda}^{-1}\mathbf{B}'$ when evaluated over $\tilde{\boldsymbol{\mu}}_L$. The computation method described here mainly focuses on an efficient implementation of the two tensors.

We need to exploit the tensor structure of the data model to simplify the implementation. Compared to the problem in [18], the new structural parameter, i.e. Doppler shift $\boldsymbol{\nu}$, is involved in several basis matrices, such as $\mathbf{B}_t$, $\tilde{\mathbf{B}}_{TV}$ and $\tilde{\mathbf{B}}_{RV}$. However if we fix the Doppler shift in the search grid $\tilde{\boldsymbol{\mu}}_L$, the problem at hand will be very similar to the one studied in [18]. With a given Doppler shift ν_{n_t} (the n_tth Doppler point), let us denote $\mathcal{T}_1^{n_t}$ and $\mathcal{T}_2^{n_t}$ as the 3D child tensors from $\mathcal{T}_1$ and $\mathcal{T}_2$. The dimension of the two new 3D tensors is $N_f \times N_R \times N_T$.

$$\mathcal{T}_1^{n_t} = \left[\left((\mathcal{Y}' \times_1 \mathbf{B}_f'^{\dagger}) \times_2 \mathbf{B}_{RV}^{n_t\prime\dagger}\right) \times_3 \mathbf{B}_{TV}^{n_t\prime\dagger}\right] \times_4 \mathbf{b}_t^{n_t\prime\dagger} \tag{60}$$

The new $\mathbf{B}$ matrices are determined by

$$\mathbf{B}_f' = \mathbf{U}_f^{\dagger}\mathbf{B}_f \tag{61}$$
$$\mathbf{B}_{RV}^{n_t\prime} = \mathbf{U}_R^{\dagger}\big(\mathbf{B}_{RV} \odot \underbrace{\big[\mathbf{A}_{t,R}(\nu_{n_t}) \ \cdots \ \mathbf{A}_{t,R}(\nu_{n_t})\big]}_{N_R}\big) \tag{62}$$
$$\mathbf{B}_{TV}^{n_t\prime} = \mathbf{U}_T^{\dagger}\big(\mathbf{B}_{TV} \odot \underbrace{\big[\mathbf{A}_{t,T}(\nu_{n_t}) \ \cdots \ \mathbf{A}_{t,T}(\nu_{n_t})\big]}_{N_T}\big) \tag{63}$$
$$\mathbf{b}_t^{n_t\prime} = \mathbf{U}_t^{\dagger}\big[e^{-j\lfloor\frac{T}{2}\rfloor\nu_{n_t}} \ e^{j(-\lfloor\frac{T}{2}\rfloor+1)\nu_{n_t}} \cdots \ e^{j(\lceil\frac{T}{2}\rceil-2)\nu_{n_t}} \ e^{j(\lceil\frac{T}{2}\rceil-1)\nu_{n_t}}\big]^T. \tag{64}$$

Similarly in terms of $\mathcal{T}_2^{n_t}$, first we reshape the diagonal elements of $\mathbf{\Lambda}^{-1}$ to form a 4D tensor $\mathcal{L}_i$, then we perform several n-mode products between $\mathcal{L}_i$ and four $\mathbf{BB}'$ matrices to acquire $\mathcal{T}_2^{n_t}$.

$$\mathcal{L}_i = \text{reshape}\big(\text{diag}\{\mathbf{\Lambda}^{-1}\}, [M_f \ M_R \ M_T \ T]\big) \tag{65}$$
$$\mathcal{T}_2^{n_t} = \left[\left((\mathcal{L}_i \times_1 (\mathbf{BB}'_f)^T) \times_2 (\mathbf{BB}_{RV}^{n_t\prime})^T\right) \times_3 (\mathbf{BB}_{TV}^{n_t\prime})^T\right] \times_4 (\mathbf{bb}_t^{n_t\prime})^T \tag{66}$$

where these special $\mathbf{BB}'$ matrices are given by

$$\mathbf{bb}_t^{n_t\prime} = \mathbf{b}_t^{n_t\prime} \odot (\mathbf{b}_t^{n_t\prime})^* \tag{67}$$
$$\mathbf{BB}'_f = \mathbf{B}'_f \odot (\mathbf{B}'_f)^* \tag{68}$$
$$\mathbf{BB}_{TV}^{n_t\prime} = \mathbf{B}_{TV}^{n_t\prime} \odot (\mathbf{B}_{TV}^{n_t\prime})^* \tag{69}$$
$$\mathbf{BB}_{RV}^{n_t\prime} = \mathbf{B}_{RV}^{n_t\prime} \odot (\mathbf{B}_{RV}^{n_t\prime})^* \tag{70}$$

APPENDIX B
JACOBIAN MATRIX AND FIM

All relevant partial derivatives in the Jacobian matrix in Eq. (29) can be found as follows

$$\frac{\partial}{\partial \boldsymbol{\tau}}\mathbf{s}(\boldsymbol{\theta}_{sp}) = \mathbf{B}_t \diamond \tilde{\mathbf{B}}_{TV} \diamond \tilde{\mathbf{B}}_{RV} \diamond \mathbf{D}_f \diamond \boldsymbol{\gamma}_{vv}^T \tag{71}$$
$$\frac{\partial}{\partial \boldsymbol{\varphi}_T}\mathbf{s}(\boldsymbol{\theta}_{sp}) = \mathbf{B}_t \diamond (\mathbf{D}_{\varphi_T,V} \odot \mathbf{A}_{t,T}) \diamond \tilde{\mathbf{B}}_{RV} \diamond \mathbf{B}_f \diamond \boldsymbol{\gamma}_{vv}^T \tag{72}$$
$$\frac{\partial}{\partial \boldsymbol{\varphi}_R}\mathbf{s}(\boldsymbol{\theta}_{sp}) = \mathbf{B}_t \diamond \tilde{\mathbf{B}}_{TV} \diamond (\mathbf{D}_{\varphi_R,V} \odot \mathbf{A}_{t,R}) \diamond \mathbf{B}_f \diamond \boldsymbol{\gamma}_{vv}^T \tag{73}$$
$$\frac{\partial}{\partial \boldsymbol{\gamma}_{vv,r}}\mathbf{s}(\boldsymbol{\theta}_{sp}) = \mathbf{B}_t \diamond \tilde{\mathbf{B}}_{TV} \diamond \tilde{\mathbf{B}}_{RV} \diamond \mathbf{B}_f \tag{74}$$
$$\frac{\partial}{\partial \boldsymbol{\gamma}_{vv,i}}\mathbf{s}(\boldsymbol{\theta}_{sp}) = j \cdot \mathbf{B}_t \diamond \tilde{\mathbf{B}}_{TV} \diamond \tilde{\mathbf{B}}_{RV} \diamond \mathbf{B}_f. \tag{75}$$

Particularly since Doppler shifts are parameters in multiple basis matrices, their partial derivatives are given by

$$\begin{aligned}\frac{\partial}{\partial \boldsymbol{\nu}}\mathbf{s}(\boldsymbol{\theta}_{sp}) = {} & \mathbf{B}_t \diamond (\mathbf{B}_{TV} \odot \mathbf{D}_{\nu,T}) \diamond \tilde{\mathbf{B}}_{RV} \diamond \mathbf{B}_f \diamond \boldsymbol{\gamma}_{vv}^T \\ & + \mathbf{B}_t \diamond \tilde{\mathbf{B}}_{TV} \diamond (\mathbf{B}_{RV} \odot \mathbf{D}_{\nu,R}) \diamond \mathbf{B}_f \diamond \boldsymbol{\gamma}_{vv}^T \\ & + \mathbf{D}_t \diamond \tilde{\mathbf{B}}_{TV} \diamond \tilde{\mathbf{B}}_{RV} \diamond \mathbf{B}_f \diamond \boldsymbol{\gamma}_{vv}^T\end{aligned} \tag{76}$$

As a summary, Tab. III provides details about the parts needed to reconstruct $\mathbf{D}(\boldsymbol{\theta}_s)$ in Eq. (30). If we take one column of

TABLE III
PARTS NEEDED TO RECONSTRUCT THE JACOBIAN MATRIX IN (30)

$\boldsymbol{\theta}_{sp}$	$\boldsymbol{\tau}$	$\boldsymbol{\varphi}_T$	$\boldsymbol{\varphi}_R$	$\boldsymbol{\nu}$	$\boldsymbol{\gamma}_{VV,r}$	$\boldsymbol{\gamma}_{VV,i}$
$\mathbf{D}_1$	$\mathbf{D}_f \diamond \boldsymbol{\gamma}_{vv}^T$	$\mathbf{B}_f \diamond \boldsymbol{\gamma}_{vv}^T$	$\mathbf{B}_f \diamond \boldsymbol{\gamma}_{vv}^T$	$\mathbf{B}_f \diamond \boldsymbol{\gamma}_{vv}^T$	$\mathbf{B}_f$	$j\mathbf{B}_f$
$\mathbf{D}_2^1$	$\tilde{\mathbf{B}}_{RV}$	$\tilde{\mathbf{B}}_{RV}$	$\mathbf{D}_{\varphi_R,V} \odot \mathbf{A}_{t,R}$	$\tilde{\mathbf{B}}_{RV}$	$\tilde{\mathbf{B}}_{RV}$	$\tilde{\mathbf{B}}_{RV}$
$\mathbf{D}_2^2$	$\tilde{\mathbf{B}}_{RV}$	$\tilde{\mathbf{B}}_{RV}$	$\mathbf{D}_{\varphi_R,V} \odot \mathbf{A}_{t,R}$	$\mathbf{B}_{RV} \odot \mathbf{D}_{\nu,R}$	$\tilde{\mathbf{B}}_{RV}$	$\tilde{\mathbf{B}}_{RV}$
$\mathbf{D}_3^1$	$\tilde{\mathbf{B}}_{TV}$	$\mathbf{D}_{\varphi_T,V} \odot \mathbf{A}_{t,T}$	$\tilde{\mathbf{B}}_{TV}$	$3(\mathbf{B}_{TV} \odot \mathbf{D}_{\nu,T})$	$\tilde{\mathbf{B}}_{TV}$	$\tilde{\mathbf{B}}_{TV}$
$\mathbf{D}_3^2$	$\tilde{\mathbf{B}}_{TV}$	$\mathbf{D}_{\varphi_T,V} \odot \mathbf{A}_{t,T}$	$\tilde{\mathbf{B}}_{TV}$	$3\tilde{\mathbf{B}}_{TV}$	$\tilde{\mathbf{B}}_{TV}$	$\tilde{\mathbf{B}}_{TV}$
$\mathbf{D}_4^1$	$\mathbf{B}_t$	$\mathbf{B}_t$	$\mathbf{B}_t$	$\mathbf{B}_t$	$\mathbf{B}_t$	$\mathbf{B}_t$
$\mathbf{D}_4^2$	$\mathbf{B}_t$	$\mathbf{B}_t$	$\mathbf{B}_t$	$\mathbf{D}_t$	$\mathbf{B}_t$	$\mathbf{B}_t$

Tab. III and plug into Eq. (30), it matches the partial derivative mentioned above.

In order to present details about all the new $\mathbf{D}$ matrices, we need to introduce a new type of derivative of the matrix $\mathbf{A}(\boldsymbol{\mu}_i) \in \mathbb{C}^{M_i \times P}$ with respect to $\boldsymbol{\mu}_i \in \mathbb{R}^{P \times 1}$, and we denote the operation by $\mathcal{D}()$.

$$\mathcal{D}(\mathbf{A}, \boldsymbol{\mu}_i) = \left[\frac{\partial}{\partial \mu_{i,1}} \mathbf{a}_1 \quad \cdots \quad \frac{\partial}{\partial \mu_{i,P}} \mathbf{a}_P \right] \tag{77}$$

Hence the new small $\mathbf{D}$ matrices in the above-mentioned partial derivatives can be expressed as

$$\mathbf{D}_f = \mathcal{D}(\mathbf{B}_f, \boldsymbol{\tau}) \tag{78}$$

$$\mathbf{D}_{\varphi_T,V} = \mathbf{G}_{TV} \cdot \mathcal{D}(\mathbf{A}, \boldsymbol{\varphi}_T) \tag{79}$$

$$\mathbf{D}_{\varphi_R,V} = \mathbf{G}_{RV} \cdot \mathcal{D}(\mathbf{A}, \boldsymbol{\varphi}_R) \tag{80}$$

$$\mathbf{D}_t = \mathcal{D}(\mathbf{B}_t, \boldsymbol{\nu}) \tag{81}$$

$$\mathbf{D}_{\nu,T} = \mathcal{D}(\mathbf{A}_{t,T}, \boldsymbol{\nu}) \tag{82}$$

$$\mathbf{D}_{\nu,R} = \mathcal{D}(\mathbf{A}_{t,R}, \boldsymbol{\nu}). \tag{83}$$

To find an alternative expression of FIM in Section III-C, we will first decompose $\mathcal{L}_i$ into a sum of outer-products of vectors based on the PARATREE model [27],

$$\mathcal{L}_i \approx \sum_{r_f=1}^{R_f} \mathbf{l}_f^{r_f} \circ \sum_{r_R=1}^{R_R} \mathbf{l}_R^{r_f,r_R} \circ \sum_{r_T=1}^{R_T} \left(\mathbf{l}_T^{r_f,r_R,r_T} \circ \mathbf{l}_t^{r_f,r_R,r_T} \right), \tag{84}$$

Based on the above approximation we can have an approximate expression for $\boldsymbol{\Lambda}^{-1}$

$$\boldsymbol{\Lambda}^{-1} = \operatorname{diag}\left\{ \operatorname{vec}(\mathcal{L}_i) \right\} \tag{85}$$

$$\approx \operatorname{diag}\left\{ \operatorname{vec}\Big(\sum_{r_f} \sum_{r_R} \sum_{r_T} \mathbf{l}_f^{r_f} \circ \mathbf{l}_R^{r_f,r_R} \circ \mathbf{l}_T^{r_f,r_R,r_T} \circ \mathbf{l}_t^{r_f,r_R,r_T} \Big) \right\} \tag{86}$$

$$= \sum_{r_f} \sum_{r_R} \sum_{r_T} \operatorname{diag}\{\mathbf{l}_t^{r_f,r_R,r_T}\} \otimes \operatorname{diag}\{\mathbf{l}_T^{r_f,r_R,r_T}\} \otimes \operatorname{diag}\{\mathbf{l}_R^{r_f,r_R}\} \otimes \operatorname{diag}\{\mathbf{l}_f^{r_f}\} \tag{87}$$

$$= \sum_{r_f} \sum_{r_R} \sum_{r_T} \boldsymbol{\Lambda}_{r_f,r_R,r_T}^{(t)} \otimes \boldsymbol{\Lambda}_{r_f,r_R,r_T}^{(T)} \otimes \boldsymbol{\Lambda}_{r_f,r_R}^{(R)} \otimes \boldsymbol{\Lambda}_{r_f}^{(f)} \tag{88}$$

Here Eq. (87) uses the property given by [27, eq. (7)].

ACKNOWLEDGMENT

The authors would like to thank Usman T. Virk, Zheda Li, Aditya Sundar, Vinod Kristem, Daoud Burghal and He Zeng for their efforts in helping the measurement campaign.

REFERENCES

[1] A. F. Molisch, *Wireless Communications*, 2nd ed. Hoboken, NJ, USA: Wiley, 2010.

[2] A. Paier *et al.*, "First results from car-to-car and car-to-infrastructure radio channel measurements at 5.2 GHz," in *Proc. IEEE 18th Int. Symp. Pers., Indoor Mobile Radio Commun.*, Sep. 2007, pp. 1–5.

[3] A. Paier *et al.*, "Car-to-car radio channel measurements at 5 GHz: Pathloss, power-delay profile, and delay-Doppler spectrum," in *Proc. IEEE 4th Int. Symp. Wireless Commun. Syst.*, Oct. 2007, pp. 224–228.

[4] L. Cheng, B. E. Henty, D. D. Stancil, F. Bai, and P. Mudalige, "Mobile vehicle-to-vehicle narrow-band channel measurement and characterization of the 5.9 GHz dedicated short range communication (DSRC) frequency band," *IEEE J. Sel. Areas Commun.*, vol. 25, no. 8, pp. 1501–1516, Oct. 2007.

[5] J. Kunisch and J. Pamp, "Wideband car-to-car radio channel measurements and model at 5.9 GHz," in *Proc. IEEE 68th Veh. Technol. Conf. (VTC-Fall)*, Sep. 2008, pp. 1–5.

[6] P. Paschalidis, A. Kortke, K. Mahler, M. Peter, M. Wisotzki, and W. Keusgen, "Wideband car-to-car MIMO radio channel measurements at 5.7 GHz in typical communication scenarios," in *Proc. IEEE 70th Veh. Technol. Conf. (VTC-Fall)*, Sep. 2009, pp. 1–5.

[7] A. F. Molisch, F. Tufvesson, J. Kåredal, and C. F. Mecklenbräuker, "A survey on vehicle-to-vehicle propagation channels," *IEEE Commun. Mag.*, vol. 16, no. 6, pp. 12–22, Dec. 2009.

[8] C. F. Mecklenbrauker *et al.*, "Vehicular channel characterization and its implications for wireless system design and performance," *Proc. IEEE*, vol. 99, no. 7, pp. 1189–1212, Jul. 2011.

[9] J. Karedal *et al.*, "A geometry-based stochastic MIMO model for vehicle-to-vehicle communications," *IEEE Trans. Wireless Commun.*, vol. 8, no. 7, pp. 3646–3657, Jul. 2009.

[10] O. Renaudin, V.-M. Kolmonen, P. Vainikainen, and C. Oestges, "Wideband measurement-based modeling of inter-vehicle channels in the 5-GHz band," *IEEE Trans. Veh. Technol.*, vol. 62, no. 8, pp. 3531–3540, Oct. 2013.

[11] T. Abbas, J. Karedal, F. Tufvesson, A. Paier, L. Bernadó, and A. F. Molisch, "Directional analysis of vehicle-to-vehicle propagation channels," in *Proc. IEEE 73rd Veh. Technol. Conf. (VTC Spring)*, May 2011, pp. 1–5.

[12] B. H. Fleury, M. Tschudin, R. Heddergott, D. Dahlhaus, and K. I. Pedersen, "Channel parameter estimation in mobile radio environments using the SAGE algorithm," *IEEE J. Sel. Areas Commun.*, vol. 17, no. 3, pp. 434–450, Mar. 1999.

[13] A. Richter, "Estimation of radio channel parameters: Models and algorithms," Ph.D. dissertation, Techn. Univ. Ilmenau, Ilmenau, Germany, May 2005. [Online]. Available: http://www.db-thueringen.de

[14] K. Levenberg, "A method for the solution of certain problems in least squares," *Quart. Appl. Math.*, vol. 2, no. 2, pp. 164–168, 1944.

[15] D. W. Marquardt, "An algorithm for least-squares estimation of nonlinear parameters," *J. Soc. Ind. Appl. Math.*, vol. 11, no. 2, pp. 431–441, 1963.

[16] J. Salmi, A. Richter, and V. Koivunen, "Detection and tracking of MIMO propagation path parameters using state-space approach," *IEEE Trans. Signal Process.*, vol. 57, no. 4, pp. 1538–1550, Apr. 2009.
[17] M. Steinbauer, A. F. Molisch, and E. Bonek, "The double-directional radio channel," *IEEE Antennas Propag. Mag.*, vol. 43, no. 4, pp. 51–63, Aug. 2001.
[18] R. Wang, O. Renaudin, R. M. Bernas, and A. F. Molisch, "Efficiency improvement for path detection and tracking algorithm in a time-varying channel," in *Proc. IEEE 82nd Veh. Technol. Conf. (VTC Fall)*, Sep. 2015, pp. 1–5.
[19] R. S. Thomä, D. Hampicke, A. Richter, G. Sommerkorn, and U. Trautwein, "MIMO vector channel sounder measurement for smart antenna system evaluation," *Trans. Emerg. Telecommun. Technol.*, vol. 12, no. 5, pp. 427–438, 2001.
[20] R. Wang, C. U. Bas, O. Renaudin, S. Sangodoyin, U. T. Virk, and A. F. Molisch, "A real-time MIMO channel sounder for vehicle-to-vehicle propagation channel at 5.9 GHz," in *Proc. IEEE Int. Conf. Commun. (ICC)*, May 2017, pp. 1–6.
[21] M. Landmann, A. Richter, and R. S. Thomä, "DoA resolution limits in MIMO channel sounding," in *Proc. IEEE Antennas Propag. Soc. Int. Symp.*, vol. 2. Jun. 2004, pp. 1708–1711.
[22] M. Landmann, M. Kaske, and R. S. Thomä, "Impact of incomplete and inaccurate data models on high resolution parameter estimation in multidimensional channel sounding," *IEEE Trans. Antennas Propag.*, vol. 60, no. 2, pp. 557–573, Feb. 2012.
[23] A. Richter, J. Salmi, and V. Koivunen, "ML estimation of covariance matrix for tensor valued signals in noise," in *Proc. IEEE Int. Conf. Acoust., Speech Signal Process. (ICASSP)*, Mar./Apr. 2008, pp. 2349–2352.
[24] A. Richter, R. Thomä, "Parametric modelling and estimation of distributed diffuse scattering components of radio channels," Prague, Czech Republic, Tech. Rep. COST 273 TD(03)198, Sep. 2003.
[25] C. B. Ribeiro, A. Richter, and V. Koivunen, "Joint angular- and delay-domain MIMO propagation parameter estimation using approximate ML method," *IEEE Trans. Signal Process.*, vol. 55, no. 10, pp. 4775–4790, Oct. 2007.
[26] B. W. Bader *et al.* (Feb. 2015). *MATLAB Tensor Toolbox Version 2.6*. [Online]. Available: http://www.sandia.gov/~tgkolda/TensorToolbox/
[27] J. Salmi, A. Richter, and V. Koivunen, "Sequential unfolding SVD for tensors with applications in array signal processing," *IEEE Trans. Signal Process.*, vol. 57, no. 12, pp. 4719–4733, Dec. 2009.
[28] J. Poutanen, J. Salmi, K. Haneda, V. Kolmonen, and P. Vainikainen, "Angular and shadowing characteristics of dense multipath components in indoor radio channels," *IEEE Trans. Antennas Propag.*, vol. 59, no. 1, pp. 245–253, Jan. 2011.
[29] A. Richter, J. Salmi, and V. Koivunen, "Distributed scattering in radio channels and its contribution to MIMO channel capacity," in *Proc. IEEE 1st Eur. Conf. Antennas Propag.*, Nov. 2006, pp. 1–7.
[30] M. Landmann, K. Sivasondhivat, J.-I. Takada, I. Ida, and R. S. Thomä, "Polarization behavior of discrete multipath and diffuse scattering in urban environments at 4.5 GHz," *EURASIP J. Wireless Commun. Netw.*, vol. 2007, no. 1, p. 057980, 2007.
[31] *IEEE Standard for Information Technology—Local and Metropolitan Area Networks—Specific Requirements—Part 11: Wireless LAN Medium Access Control (MAC) and Physical Layer (PHY) Specifications Amendment 6: Wireless Access in Vehicular Environments*, IEEE Standard 802.11p-2010 (Amendment to IEEE Std 802.11-2007 as amended by IEEE Std 802.11k-2008, IEEE Std 802.11r-2008, IEEE Std 802.11y-2008, IEEE Std 802.11n-2009, and IEEE Std 802.11w-2009), Jul. 2010, pp. 1–51, doi: 10.1109/IEEESTD.2010.5514475.
[32] L. De Lathauwer, B. De Moor, and J. Vandewalle, "A multilinear singular value decomposition," *SIAM J. Matrix Anal. Appl.*, vol. 21, no. 4, pp. 1253–1278, 2000.

Rui Wang received the B.S. degree from Southeast University, Nanjing, China, in 2010, and the M.S. degree (Hons.) from the University of Southern California, Los Angeles, CA, USA, in 2012, where he is currently pursuing the Ph.D. degree with the WiDeS Group, Ming-Hsieh Department of Electrical Engineering. His research interests include wireless channel measurements and modeling for vehicle-to-vehicle, mm-wave communication systems, and high-resolution parameter extraction algorithms for channel measurement evaluation.

Olivier Renaudin received the M.Sc. degree in electrical engineering from Université Bordeaux I, France, in 2006, and the Ph.D. degree in electrical engineering from Université catholique de Louvain, Louvain-la-Neuve, Belgium, in 2013. From 2014 to 2016, he was with the Wireless Devices and Systems Group, University of Southern California, Los Angeles, CA, USA, as a Post-Doctoral Researcher. He is currently a Research Scientist with the Austrian Institute of Technology, Vienna, Austria.

C. Umit Bas received the B.Sc. and M.Sc. degrees in electrical and electronics engineering from Koc University, Istanbul, Turkey, in 2010 and 2012, respectively. He is currently pursuing the Ph.D. degree with the Department of Electrical Engineering, University of Southern California, Los Angeles, CA, USA. His research interests include real-time channel sounders for mm-wave and UWB communications and wireless propagation channel measurements and modeling.

Seun Sangodoyin received the B.Sc. degree in electrical engineering from Oklahoma State University in 2007, and the M.Sc. degree in electrical engineering from the University of Southern California in 2009, where he is currently pursuing the Ph.D. degree in electrical engineering. His research interest includes measurement-based MIMO channel modeling and analysis, UWB MIMO radar, parameter estimation, body area networks, and stochastic dynamical systems.

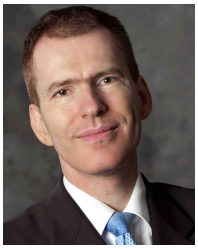

Andreas F. Molisch (S'88–M'95–SM'00–F'05) received the Dipl.-Ing., Ph.D., and Habilitation degrees from the Technical University of Vienna, Vienna, Austria, in 1990, 1994, and 1999, respectively. He subsequently was with AT&T (Bell) Laboratories, USA, Lund University, Lund, Sweden, and Mitsubishi Electric Research Labs, USA. He is currently a Professor and the Solomon-Golomb–Andrew-and-Erna-Viterbi Chair at the University of Southern California, Los Angeles, CA, USA. His current research interests are the measurement and modeling of mobile radio channels, multiantenna systems, ultra-wideband communications and localization, novel modulation and multiple access systems, and wireless video distribution. He has authored, coauthored, or edited four books (among them the textbook *Wireless Communications*, Wiley–IEEE Press), 19 book chapters, over 200 journal papers, 300 conference papers, and over 80 patents and 70 standards contributions. He has been an editor of a number of journals and special issues, the general chair, the technical program committee chair, or the symposium chair of multiple international conferences, and the chairman of various international standardization groups. He is a Fellow of the National Academy of Inventors, a Fellow of the AAAS, a Fellow of the IET, an IEEE Distinguished Lecturer, and a Member of the Austrian Academy of Sciences. He has received numerous awards, among them the Donald Fink Prize of the IEEE and the Eric Sumner Award of the IEEE.